A Supervised Approach for Estimating Fractional Abundances of Binary Intimate Mixtures

Bikram Koirala ⬤ , *Member, IEEE*, Behnood Rasti ⬤ , *Senior Member, IEEE*,
and Paul Scheunders ⬤ , *Senior Member, IEEE*

Abstract—**In this work, we propose a supervised framework for spectral unmixing of binary intimate mixtures. The core idea is based on geodesic distance measurements and regression to estimate the fractional abundances. The main assumption is that spectral reflectances of binary mixtures form a curve between the two endmembers, and the mixture's relative position on this curve serves as an indicator of its fractional abundances. We propose four novel approaches to approximate this relative position. From this, the fractional abundances are obtained using Gaussian process regression. The proposed framework simultaneously copes with the spectral variability by hypersphere and high-dimensional simplex projections. The approach is extensively validated on real datasets, including binary mineral mixtures and industrial clay powder mixtures produced in a laboratory setting, comprising 60 binary mixtures derived from five types of clay powders: kaolin, roof clay, red clay, mixed clay, and calcium hydroxide, measured by a variety of hyperspectral sensors in the VNIR–SWIR and mid-and long-wave infrared regions. A comparison with the linear mixing model and several nonlinear mixing models demonstrates the superiority of the proposed approach.**

Index Terms—**Hyperspectral, spectral variability, nonlinearity, mixing models, mineral powder mixtures.**

I. INTRODUCTION

HYPERSPECTRAL unmixing aims at estimating the fractional contributions (abundances) of various pure materials (endmembers) within a pixel's field of view. Generally, spectral unmixing is carried out by formulating a mathematical model that characterizes spectral reflectance as a function of endmembers and their fractional abundances. Subsequently, the inversion of this model provides an estimation of the composition of pixels. The linear mixing model (LMM) [1] is the most widely used model in the remote sensing community. The major assumption of this model is that each incident light ray interacts with a single pure material within the pixel's instantaneous field of view before reaching the sensor. As the fractional abundance represents the extent of ground coverage by each pure material, the fully constrained least squares unmixing procedure (FCLSU) [2], [3] estimates these abundances while taking into account their physical constraints, i.e., they should be nonnegative and sum up to one. The LMM is commonly favored in scenarios where the Earth's surface exhibits extensive flat, well-defined, and distinct regions containing different endmembers.

Due to the success of deep learning in computer vision and image recognition tasks, there has been a recent trend of integrating deep autoencoder architectures with the LMM. The basic idea of these structures is to map the input hyperspectral image into fractional abundances. This is generally done by utilizing the encoder, while the decoder transforms the estimated fractional abundances into reconstructed hyperspectral images using linear layers, where the endmembers act as the weights. A variety of autoencoders has been applied in hyperspectral unmixing: denoising autoencoders [4], sparse nonnegative autoencoders [5], variational autoencoders [6], [7], convolutional autoencoders [8], [9], [10], [11], adversarial autoencoders [12], [13], and transformer autoencoders (see [14], [15]).

The LMM is not suitable when hyperspectral images are acquired from the Earth's surface scenes featuring complex geometric structures. In these scenarios, each incident ray of light interacts with multiple pure materials in the scene before reaching the sensor. This results in a nonlinear relationship between the fractional abundances and the measured reflectance spectra. To describe the interaction of light with complex geometric structures, nonlinear mixing models have been proposed [16].

A widely used group of nonlinear mixing models are bilinear mixing models. The major assumption of these models is that an incident ray of light interacts with a maximum of two pure materials before reaching the sensor. These models often have a nonlinear term in addition to the linear term. The Fan model [17] derives this nonlinear term through the first-order Taylor series expansion of a general nonlinear mixing equation. Because of the hard nonlinear constraint, this model cannot perform well on datasets that follow the LMM. To generalize bilinear mixing models to the linear case, the generalized bilinear model [18], the polynomial postnonlinear mixing model (PPNM) [19], and the linear-quadratic model [20] have been proposed. These models have hyperparameters to balance between linear and nonlinear terms. To describe higher order interactions of the incident ray of light before reaching the sensor, the multilinear mixing model

(MLM) [21] and the p-linear ($p > 2$) mixture model [22], [23], [24], etc., have been proposed.

The aforementioned approaches all use a mathematical formulation to describe the unmixing problem. Another group of mixing models has been developed based on physics-based radiative transfer principles. These models are often utilized to describe the spectral reflectance of intimate mineral powder mixtures. In remote sensing applications, the Hapke model [25], [26] is extensively utilized. This model assumes that the particles of the intimate mixtures are significantly larger than the wavelength of light, are spherical, and scatter light isotropically.

A limited number of studies exploit the potential of deep learning for nonlinear unmixing. Deep autoencoder architectures have been developed that utilize the PPNM to reconstruct the input hyperspectral image [27], [28]. In [29], it was demonstrated that the endmembers of nonlinear datasets can be accurately estimated through the use of deep autoencoder architectures.

Rather than relying on a specific mixing model for spectral unmixing, efforts have been made to learn the nonlinearity inherent in a dataset through a data-driven approach [30], [31], [32], [33]. The major disadvantage of these approaches is their limited generalization capacity. In [34], it was shown that these methods encounter complete failure when test and training samples lie on different data manifolds, due to variations in acquisition and illumination conditions. Variations in illumination conditions often lead to scaling effects, either globally or on a pixel-based level, in the measured spectral data. On the other hand, variations in acquisition conditions, such as differences in sensors and white calibration contribute to wavelength-dependent variations in the measured spectra. These phenomena are often referred to as external spectral variability [34], [35]. Even though the intrinsic nonlinearity of a dataset does not change with global scaling [34], also the existing nonlinear mixing models are not invariant to external variability, due to the fact that the nonlinear function transforms any scaling effect nonlinearly.

In linear spectral unmixing, external spectral variability has been tackled by methods based on endmember bundles (see [36], [37], [38]), physical (see [39], [40], [41]), and statistical models (see [42], [43], [44]). To bridge the gap between endmember bundle-based methods and parametric physics-based models, in [45], a multiple endmember mixing model was proposed.

The aforementioned nonlinear models do not take into account the spectral variability. In the works of [46] and [47], bilinear models were expanded by introducing a scaling term to specifically tackle external spectral variability. In [48], the impact of spectral variability in bilinear models has been modeled by a normal distribution. In the study by Siebels et al. [49], an approach named neighbor-band ratio unmixing (NBRU) was introduced to estimate fractional abundances from intimate mineral powder mixtures, and its resilience against external spectral variability was validated. In general, the inversion of a model that simultaneously tackles spectral variability and nonlinearity tends to be highly nonconvex. These models often have a substantial number of hyperparameters, leading to challenges in terms of optimization and interpretation.

In this work, we proposed a supervised methodology for unmixing of binary intimate powder mixtures. This methodology assumes that spectral reflectances of binary mixtures form a curve between the two endmembers, and the mixture's relative position on this curve serves as an indicator of its fractional abundances. In practical scenarios, variations in illumination conditions may cause the spectra of mixtures to deviate from the curve. To address this challenge, we will investigate two distinct projections designed to make the data scale-invariant. When identical binary mixtures are captured using different sensors, different curves are obtained, but the relative position on these curves constitutes a unique representation of the mixture's composition. In [34], the relative position of the mixture is approximated by estimating the geodesic distances between a mixture and the endmembers, by sampling the curve with a large number of mixtures. In practice, only one mixture and the two endmembers are generally available. In this study, we will investigate two approaches to estimate the relative position of a mixture solely based on the mixture and both endmembers. It is important to note that these approaches assume that both the spectra of the mixture and the endmembers are acquired using the same sensor.

Because mixtures with equidistant abundances are not equidistant on the curve, a nonlinear relation exists between the relative position and actual fractional abundances [34]. To learn this relationship, a supervised nonlinear regression approach will be employed. The supervised method will be trained using training samples obtained from a particular acquisition scenario (e.g., a dataset acquired by one specific sensor).

Contributions and novelties: The contributions of the proposed research are as follows.

1) In this work, we proposed four different supervised approaches for estimating the fractional abundances of binary intimate mixtures. These approaches involve the integration of two projection methods and two distinct relative position estimation methods.

2) *Simultaneous tackling nonlinearity and spectral variability:* The proposed approach not only characterizes the nonlinearity of intimate mixtures but also finds a unique representation of binary intimate mixtures to tackle the spectral variability.

3) *Comprehensive analysis of binary intimate mixture samples:* We validated the proposed approach on a large amount of binary intimate mixtures acquired by a large variety of sensors, with a broad wavelength range between the visible and the long-wavelength infrared regions (i.e., between 350 and 15 385 nm).

4) In the experimental section, we demonstrated that the analysis of intimate mixtures from spectral reflectance is challenging and reveals highly inaccurate results from linear and nonlinear mixing models.

The rest of this article is organized as follows. Section II provides a detailed explanation of the proposed methodology. In Section III, we describe three real intimate powder mixture datasets on which our methodology is validated. In Section IV, we outline the experiments and present the results, followed by

a discussion in Section V. Finally, Section VI concludes this article.

II. METHODOLOGY

It is generally assumed that the spectral reflectance of intimate mixtures $\mathbf{X}(\{\mathbf{x}_i\}_{i=1}^N \in \mathbf{R}_+^d)$ can be described by the nonlinear combination of endmembers $\mathbf{E}(\{\mathbf{e}_j\}_{j=1}^p \in \mathbf{R}_+^d)$ and their fractional abundances $\mathbf{A}(\{\mathbf{a}_i\}_{i=1}^N \in \mathbf{R}_+^p)$

$$\mathbf{x}_i = F(\mathbf{E}, \mathbf{a}_i) + \boldsymbol{\eta}_i \tag{1}$$

where p denotes number of endmembers, d denotes spectral bands, F is a nonlinear function, and $\boldsymbol{\eta}_i$ represents Gaussian noise.

Our framework estimates the fractional abundances of binary intimate mixtures with known endmembers. The proposed framework contains the following three main steps: projection, relative position estimation, and abundance estimation. We propose two projection approaches (i.e., hypersphere and simplex projection) and two relative distance estimation approaches (geodesic and projection unmixing).

A. Hypersphere Projection

The first projection that makes the spectra invariant to scaling is the projection onto the unit hypersphere. The projection of a vector $(\mathbf{x})$ onto the unit hypersphere is achieved by dividing the vector by its length $(\mathbf{y} = \mathbf{x}/\sqrt{\sum_{i=1}^d x_i^2})$. On a unit (hyper)sphere, the arc length between any 2 unit-length vectors equals the angle between them. The cosine of the angle is given by the dot product between them. In this way, the arc length (T) between two endmembers on the unit hypersphere can be computed by taking the arc cosine of their dot product: $T = \arccos(\mathbf{e_1}^T\mathbf{e_2})$, where the length of vectors $\|\mathbf{e_1}\| = 1$ and $\|\mathbf{e_2}\| = 1$. When a mixture lies on the arc connecting the 2 endmembers ($\mathbf{y}'$ as an example in Fig. 1), the geodesic distance between the mixture and the endmembers is obtained by: $b_1 = \arccos(\mathbf{e_1}^T\mathbf{y}')$ and $b_2 = \arccos(\mathbf{e_2}^T\mathbf{y}')$. However, in reality the mixtures lie on a curve between the endmembers that can substantially deviate from the arc. In Fig. 1, we illustrate a scenario wherein the spectrum of a binary mixture, represented by $\mathbf{y}$, deviates from the arc connecting the two endmembers $\mathbf{e_1}$ and $\mathbf{e_2}$ (as indicated by the red curve).

By employing the law of cosines

$$\cos(c_1) = \cos(d)\cos(b_1)$$
$$\cos(c_2) = \cos(d)\cos(b_2) \tag{2}$$

one can obtain the arc lengths b_1 and b_2 of $\mathbf{y}'$, the projected data point on the arc connecting the two endmembers (for further details, we refer to [50])

$$b_1 = \arccos\left(\frac{\sin(T)}{\sqrt{\left[\left[\frac{\cos(c_2)}{\cos(c_1)} - \cos(T)\right]^2 + \sin^2(T)\right]}}\right) \tag{3}$$

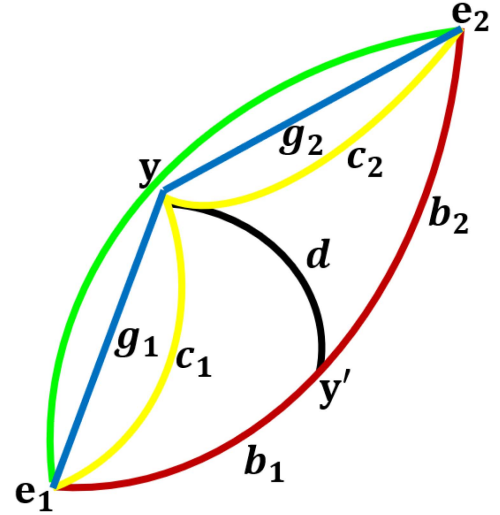where $T = b_1 + b_2 = \arccos(\mathbf{e_1}^T\mathbf{e_2})$.

Fig. 1. Red curve: The arc connecting the two endmembers. Yellow curves: The arcs connecting the binary mixture ($\mathbf{y}$) with both endmembers; c_1 and c_2 denote the arc lengths between $\mathbf{y}$ and the endmembers $\mathbf{e_1}$ and $\mathbf{e_2}$, respectively. $\mathbf{y}'$ represents the projection of $\mathbf{y}$ on the arc, while b_1 and b_2 denote the arc lengths between $\mathbf{y}'$ and the endmembers. Green curve: The true curve that connects the endmembers; g_1 and g_2 denote the Euclidean distances between $\mathbf{y}$ and the endmembers.

1) Hypersphere Projection Unmixing (HPU): The mixture's relative position on the arc connecting the endmembers is given by

$$\hat{\mathbf{a}} = \begin{bmatrix} \frac{b_2}{b_1+b_2} \\ \frac{b_1}{b_1+b_2} \end{bmatrix}. \tag{4}$$

We will refer to this methodology as HPU.

2) Hypersphere Geodesic Unmixing (HGU): However, when the actual curve of the mixtures (the green curve in Fig. 1) substantially deviates from the arc between the endmembers, the true geodesic distance might deviate a lot from the arc length. The only option remaining is to approximate the geodesic distances by the Euclidean distances (g_1 and g_2) to obtain the mixture's relative position

$$\hat{\mathbf{a}} = \begin{bmatrix} \frac{g_2}{g_1+g_2} \\ \frac{g_1}{g_1+g_2} \end{bmatrix}. \tag{5}$$

We will refer to this methodology as HGU. In the simulation experiment, we will demonstrate that, even though this approximation can deviate substantially from the true geodesic distance, the estimated relative positions obtained from (5) closely resemble those derived from the true geodesic distance.

B. High-Dimensional Simplex Projection

The second projection that makes the spectra invariant to scaling is the projection of data point $(\mathbf{x})$ onto a high-dimensional simplex, by dividing each element of the vector by the sum of all its elements $(\mathbf{y} = \mathbf{x}/\sum_{i=1}^d x_i)$. Unlike the unit hypersphere, this space is a linear space. When the mixture lies on the line connecting the 2 endmembers, the relative position of the mixture is simply given by its Euclidean distances from the
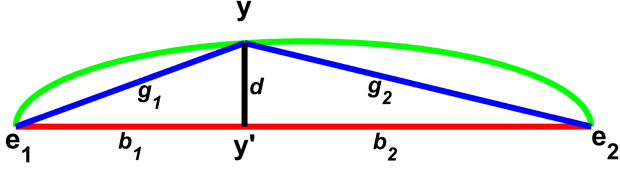
Fig. 2. Red line: Line connecting the two endmembers. Blue lines: Lines connecting the binary mixture ($\mathbf{y}$) with the endmembers. $\mathbf{y}'$ represents the projection of $\mathbf{y}$ on the line, b_1 and b_2 denote the Euclidean distances between $\mathbf{y}'$ and the endmembers. Green curve: The true curve that connects the endmembers. g_1 and g_2 denote the Euclidean distances between $\mathbf{y}$ and the endmembers.

endmembers. However, the real curve between the endmembers may deviate from the line connecting the two endmembers. In Fig. 2, we illustrate a scenario wherein the spectrum of a binary mixture, represented by $\mathbf{y}$, deviates from the line connecting the two endmembers $\mathbf{e_1}$ and $\mathbf{e_2}$ (as indicated by the red line).

By utilizing the Pythagorean theorem

$$g_1^2 = d^2 + b_1^2$$
$$g_2^2 = d^2 + b_2^2 \qquad (6)$$

one can obtain the Euclidean distances of the projected data point $\mathbf{y}'$ on the red line

$$b_1 = \left(\frac{(b_1 + b_2)^2 + g_1^2 - g_2^2}{2(b_1 + b_2)} \right) \qquad (7)$$

where $b_1 + b_2 = \|\mathbf{e_1} - \mathbf{e_2}\|$.

1) Simplex Projection Unmixing (SPU): For SPU, the relative position of the mixture is then given by (4). We will refer to this method as SPU.

2) Simplex Geodesic Unmixing (SGU): However, when the actual curve of the mixtures (the green curve in Fig. 2) substantially deviates from the line between the endmembers, the result of SPU might deviate from the true relative position. The only option remaining is to approximate the geodesic distances on the curve by the Euclidean distances g_1 and g_2 to obtain the mixture's relative position [see (5)]. We will refer to this method as SGU.

C. Abundance Estimation Using Supervised Regression

Due to the nonequidistant nature of mixtures with equidistant abundances on the curve, a nonlinear relationship emerges between the relative position and actual fractional abundances. To model this intricate relationship, we will adopt a supervised nonlinear regression approach. The supervised method will undergo training using samples derived from a specific acquisition scenario, such as a dataset acquired by a particular sensor. The actual abundances are obtained by minimizing the following optimization equation:

$$\mathbf{a} = \arg\min_{\mathbf{a}} \left\| F(\hat{\mathbf{a}}) - \mathbf{Ea} \right\|^2$$

$$\text{s.t.} : \sum_{l=1}^{p} a_l = 1 \quad \forall l : a_l \geq 0 \qquad (8)$$

Algorithm 1: Supervised Approach for Estimating Fractional Abundances of Binary Intimate Mixtures.

Input: $\mathbf{Y}^{\text{train}}(\{\mathbf{y}_i\}_{i=1}^N \in \mathbf{R}_+^d)$, $\mathbf{E}^{\text{train}}(\{\mathbf{e}_l\}_{l=1}^2 \in \mathbf{R}_+^d)$,
$\qquad \mathbf{Y}^{\text{test}}(\{\mathbf{y}_i\}_{i=1}^M \in \mathbf{R}_+^f)$, $\mathbf{E}^{\text{test}}(\{\mathbf{e}_l\}_{l=1}^2 \in \mathbf{R}_+^f)$
Output: $\hat{\mathbf{A}}^{\text{test}}(\{\mathbf{a}_i\}_{i=1}^M \in \mathbf{R}_+^2)$
Determining the relative position of the mixture (Begin)
   Estimate the relative position of the mixture by applying one of the following two equations: (4) and (5)
Determining the relative position of the mixture (End)
Training the supervised model (Begin)
   Estimating hyperparameters involved in (9) (see [34] for the detailed explanation)
Training the supervised model (End)
for $o \leftarrow 1$ **to** M
   $\hat{\mathbf{A}}_o^{\text{test}} := $ Estimate the fractional abundance of each test sample by applying (8)

---

where the function $F(\cdot)$ can be estimated by using Gaussian processes regression, for further details, we refer to [34], [51]

$$F(\hat{\mathbf{a}}) = \mathbf{EA}(K(\hat{\mathbf{A}}, \hat{\mathbf{A}}) + \sigma_n^2 \mathbf{I})^{-1} K(\hat{\mathbf{a}}, \hat{\mathbf{A}})^T \qquad (9)$$

where the matrix $\hat{\mathbf{A}}(\{\hat{\mathbf{a}}_i\}_{i=1}^N \in \mathbf{R}_+^p)$ contains the estimated relative positions of the training set and the matrix $\mathbf{A}$ refers to its ground truth fractional abundances. The kernel function (K) involved in (9) is the squared exponential kernel function and σ_n^2 is the noise variance of the estimated relative positions. The pseudocode of the proposed method is shown in Algorithm 1.

III. HYPERSPECTRAL DATA

A. Relab Dataset

The dataset comprises spectra derived from carefully prepared mineral mixtures at the NASA Reflectance Experiment Laboratory (RELAB) at Brown University [52]. The chosen binary mixtures involve the following five minerals: alunite (Al), anorthite (An), bronzite (Br), olivine (Ol), and quartz (Qz). Each binary combination, namely An–Br, Br–Ol, Ol–An, and Qz–Al, comprises three mixtures characterized by mass ratios of approximately 25%, 50%, and 75%. Notably, these minerals share similar grain sizes (around 100 μm) and densities (approximately 3 g/cm^3), resulting in volumetric and areal fractional abundances closely mirroring these mass ratios. Fig. 3 shows the endmembers from the Relab dataset. The rationale for selecting this dataset lies in the accurate estimation of the mixture's fractional abundances by the Hapke model.

B. Self-Crafted Mineral Dataset

In earlier work [34], we generated datasets comprising homogeneously mixed mineral powder combinations acquired by two sensors: an AgriSpec spectroradiometer [manufactured by analytical spectral devices (ASD)] and a Snapscan shortwave infrared hyperspectral camera. The selected minerals are various oxides commonly found in soil and utilized in cementitious materials, namely aluminum oxide (Al$_2$O$_3$), calcium hydroxide
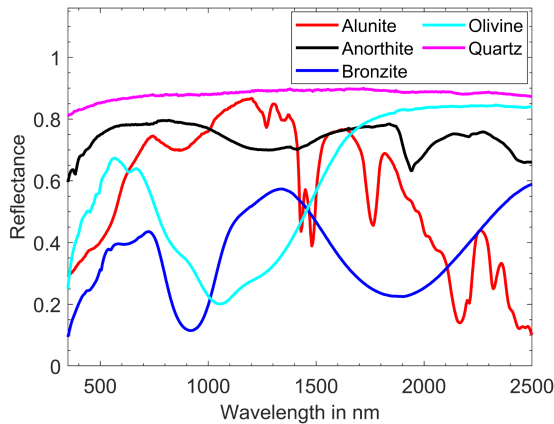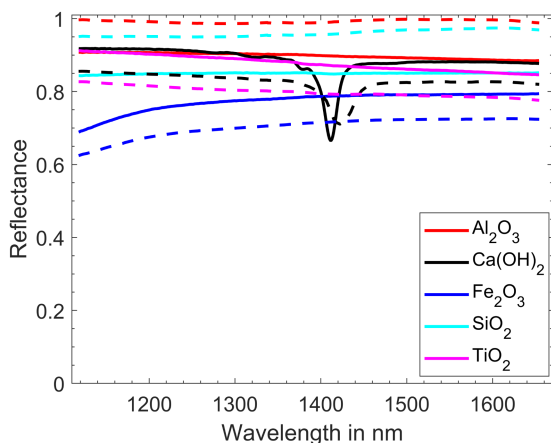
Fig. 3. Endmembers from the relab dataset.

Fig. 4. Spectral reflectance of pure mineral powders (endmembers) acquired by the ASD spectroradiometer (full line) and the hyperspectral camera (dashed).

$(Ca(OH)_2)$, iron oxide (Fe_2O_3), silicon dioxide (SiO_2), and titanium dioxide (TiO_2).

From these minerals, seven binary mixture combinations were prepared: Al_2O_3–SiO_2 (Al–Si), $Ca(OH)_2$–SiO_2 (Ca–Si), $Ca(OH)_2$–TiO_2 (Ca–Ti), Fe_2O_3–Al_2O_3 (Fe–Al), Fe_2O_3–$Ca(OH)_2$ (Fe–Ca), Fe_2O_3–SiO_2 (Fe–Si), and SiO_2–TiO_2 (Si–Ti). Within each mineral combination, 7 samples were generated with ground truth fractional abundances exhibiting uniform variation, spanning mass ratios from 12.5% to 87.5%. We transformed mass ratios into volume ratios by utilizing the densities of the pure mineral powders. Fig. 4 illustrates the spectra of the pure mineral powders acquired by both the ASD spectroradiometer and the hyperspectral camera. Noticeable distinctions in the obtained spectra arise from external factors, encompassing variations in illumination, sample-to-sensor distances leading to global scaling effects, and sensor-related differences like the utilization of different white calibration procedures, resulting in wavelength-dependent scaling.

C. Multisensor Hyperspectral Benchmark Dataset

In recent work [53], a comprehensive laboratory ground truth dataset of intimately mixed mineral powders was created. This involved homogeneously mixing five clay powders (kaolin, roof clay, red clay, mixed clay, and $Ca(OH)_2$) to generate a total of 325 samples, including 60 binary, 150 ternary, 100 quaternary, and 15 quinary mixtures. These 325 mixtures and five pure clay powders were scanned by eight different sensors across the visible (V), near-infrared (NIR), and short-wave infrared (SWIR) wavelength regions, and three sensors in the mid-wave infrared (MWIR) and long-wave infrared (LWIR). The properties of all the sensors are summarized in Table I. To maintain consistency with the first two datasets, this study will exclusively concentrate on the 60 binary mixtures.

Figs. 5 and 6 depict the spectra of the pure clay powders acquired by the aforementioned sensors. It is noteworthy that considerable spectral variability occurs in the obtained spectra. The observed variations arise from differences in illumination and acquisition conditions, the utilization of various white calibration panels, and specific dissimilarities in the spectral response functions of the sensors.

IV. EXPERIMENTAL RESULTS

Here, the results of HPU, HGU, SPU, and SGU are compared with four different mixing models (i.e., FCLSU [2], [3], PPNM [19], MLM [21], and the Hapke model [25], [26]) and the NBRU approach NBRU [49]. For all of these methods, endmembers are acquired by the hyperspectral sensors. For HPU, HGU, SPU, and SGU, a mapping between the relative position and the LMM is learned by using the training samples obtained from one of the applied sensors.

Quantitative comparisons are expressed through the abundance root mean squared error (AE), representing the discrepancy between the estimated fractional abundances ($\hat{A}$) and the ground truth fractional abundances (A)

$$\text{Abundance RMSE (AE)} = \sqrt{\frac{1}{pn}\sum_{k=1}^{p}\sum_{i=1}^{n}\left(\hat{A}_{ki} - A_{ki}\right)^2} \times 100 \tag{10}$$

where p and n denote the number of endmembers and the number of mixed spectra, respectively.

A. Simulation Experiment

In this experiment, we aim to showcase that the relative position of a data point on a nonlinear curve, estimated by the proposed approach does not differ much from the true geodesic distance. As nonlinear curves, we choose a circle, an exponential curve, a parabola, as well as datasets generated by the Hapke model and the Fan model. We sampled the curves with 1000 datapoints, with corresponding uniformly sampled fractional abundances. For the mixing models, a total of 1000 binary mixtures were generated by combining Qz and Al (see Fig. 3 for their spectral reflectances). The true curve lengths between the endmembers were estimated by summing up the Euclidean distances between neighboring samples on the 1-nearest neighbor graph. For this, all 1000 data points were applied. Then, the length was approximated by summing up the Euclidean distances between one binary mixture and the two endmembers. Given that the error in the approximated geodesic distance is

TABLE I
OVERVIEW OF THE SENSORS UTILIZED IN THIS STUDY

| Sensor	Spectral range	Bands/Channels	Spatial resolution	Spectral resolution
ASD Spectroradiometer	$350 - 2500$ nm	2151	-	$3 - 6$ nm
PSR-3500 spectral evolution	$350 - 2500$ nm	1024	-	$2.8 - 8$ nm
Specim AisaFenix	$400 - 2500$ nm	450	1024 pixels	$3.5 - 10$ nm
IMEC hyperspectral camera	$1120 - 1675$ nm	100	400×400 pixels	5 nm
Specim sCMOS	$400 - 1000$ nm	238	2148 pixels	6 nm
Cubert Ultris X20P	$350 - 1000$ nm	164	410×410 pixels	4 nm
Senops HSC2	$500 - 900$ nm	50	1024×1024 pixels	$10 - 16$ nm
Specim JAI(RGB)	$440 - 630$ nm	3	4096×8496 pixels	-
Specim FX50	$2700 - 5300$ nm	308	640 pixels	35 nm
Specim AisaOwl	$7600 - 12300$ nm	96	385 pixels	100 nm
Agilent 4300 FTIR	$2500 - 15385$ nm	7191	-	$4 - 16$ cm^{-1}
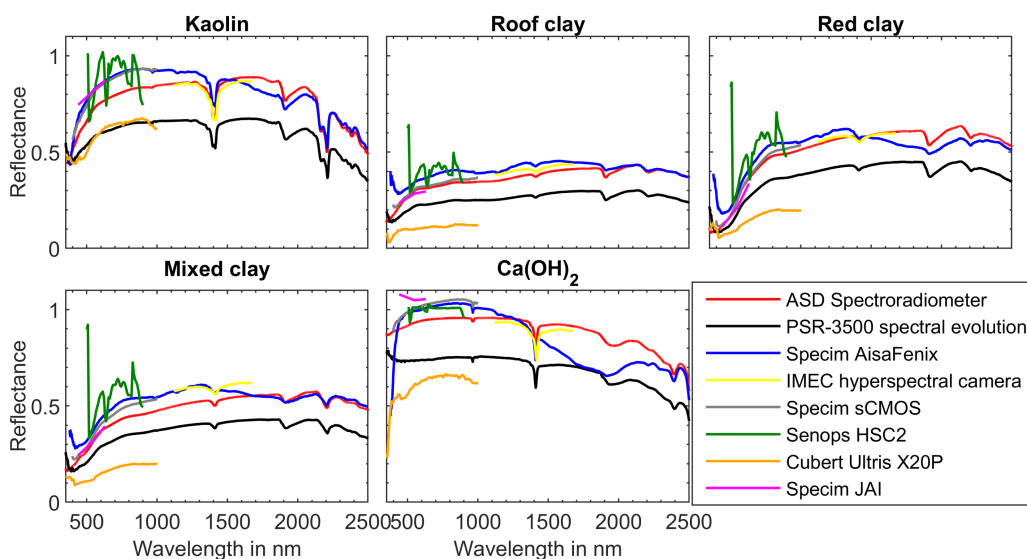
Fig. 5.   Spectra of pure clay samples acquired by eight different sensors in the VNIR and SWIR.
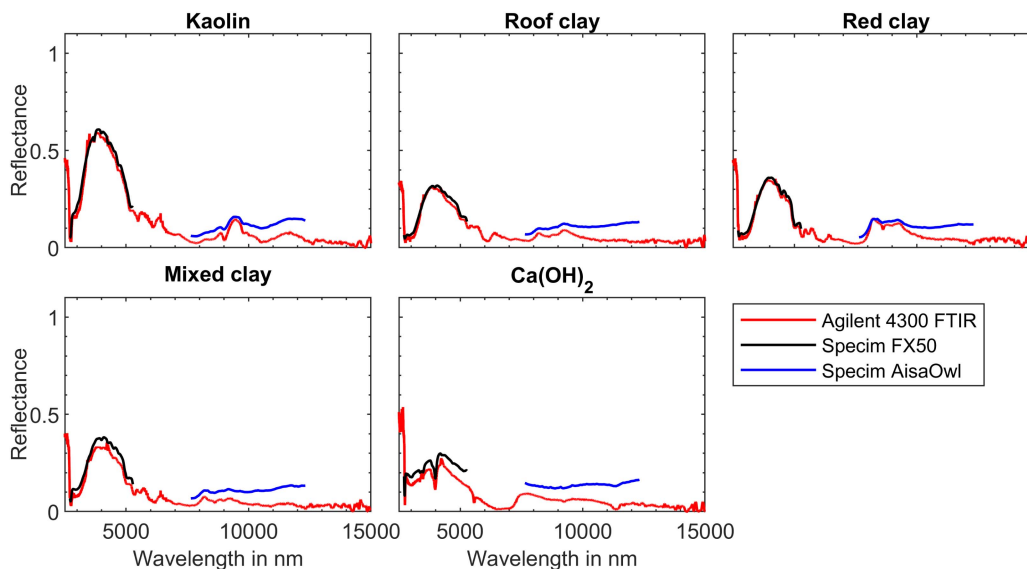

Fig. 6.   Spectra of pure clay samples acquired by three different sensors in the MWIR and LWIR.

TABLE II
NONLINEAR CURVES AND THE ASSOCIATED APPROXIMATION ERRORS

Model	Equation	True length	Approximated length	Error in length (in %)	Error in relative position (in %)
Circle	$\mathbf{y} = \begin{bmatrix} \cos(\theta) \\ \sin(\theta) \end{bmatrix}, 0 \le \theta \le \pi/2$	1.57	1.49±0.04	5.10	0.73
Exponential	$\mathbf{y} = \begin{bmatrix} exp(1-a) \\ \exp(a) \end{bmatrix}, 0 \le a \le 1$	2.52	2.48±0.02	1.61	0.28
Parabola	$\mathbf{y} = \begin{bmatrix} a \\ a^2 \end{bmatrix}, 0 \le a \le 1$	1.48	1.45±0.02	2.02	0.52
FM	$\mathbf{y} = \mathbf{y} + \sum_{m=1}^{p-1} \sum_{k=m+1}^{p} a_m a_k \mathbf{e}_m \odot \mathbf{e}_k$ $\mathbf{y} = \sum_{i=1}^{p} a_i \mathbf{e}_i$	9.35	9.03±0.15	3.42	0.70
Hapke	$y = \frac{\mathbf{Wa}}{(1+2\cos(\theta_e)\sqrt{1-\mathbf{Wa}})(1+2\cos(\theta_i)\sqrt{1-\mathbf{Wa}})}$	8.97	8.81±0.06	1.78	0.25

TABLE III
AE OF ALL METHODS ON THE BINARY INTIMATE MIXTURES OF THE RELAB DATASET

	FCLSU	PPNM	MLM	Hapke	NBRU	HPU	HGU	SPU	SGU
An–Br	19.50	22.61	19.50	**1.03**	4.95	1.46	1.47	1.47	1.48
Br–Ol	16.13	13.95	13.05	1.21	3.61	0.76	1.14	**0.74**	1.13
Ol–An	13.65	13.20	11.21	2.39	3.89	2.07	**2.01**	2.08	2.03
Qz–Al	24.73	26.25	24.73	3.57	14.48	**1.71**	1.83	**1.71**	1.81

The best performances are shown in bold.

dependent on the position of the binary mixture on the curve, we conducted 1000 approximations by gradually altering the binary mixture. The mean of these approximations was then obtained as the approximated curve length. In Table II, we show the true lengths of these curves, the mean approximated lengths of the curves ($\pm$ standard deviation), the errors in the obtained lengths and the errors in the relative position of data points on the curve due to the approximation. As can be observed, despite significant deviations in the estimated length of the curves (1.6%–5.1%), the impact on the estimated relative position of data points on the curve was limited (error below 1%).

B. Experiment on Relab Dataset

Since HPU, HGU, SPU, and SGU require training samples to learn the nonlinearity of the dataset, the Hapke model was utilized to simulate the spectral reflectances of a large number of binary mixtures. For each binary combination, a total of 100 mixtures with uniformly distributed fractional abundances was generated. These spectra were then utilized to learn a mapping between the relative positions and the fractional abundances of the mixtures.

Table III shows the results obtained by applying different spectral unmixing techniques to the real Relab binary mixtures. As expected, except for the Hapke model, none of the mixing models could perform well for this dataset. An interesting observation is that NBRU performed reasonably well for all binary mixtures, except for the Qz–Al combination. All four methods proposed in this work perform well on all mixtures, and even showed a better performance than the Hapke model on the binary mixtures of Br–Ol, Ol–An, and Qz–Al. The observed superiority of the proposed method over the Hapke model can be partly attributed to the potential existence of a scaling effect in the spectral reflectances of the mixtures. As previously highlighted, mixing models, and thus, also the Hapke model cannot deal with random scaling effects occurring in measured spectra.

C. Experiment on Self-Crafted Mineral Dataset

For this dataset, the Hapke model performs not well, and cannot be used to learn the mapping between the relative position and the abundances. Instead, the spectroradiometer dataset is used for training of the supervised approaches. The performance of the mixing models and the proposed methods was validated on the camera data.

Table IV shows the results obtained by applying the different mixing models and the proposed methods to the camera dataset. Due to the complexity of this dataset, none of the mixing models performed well. Even though the Hapke model is designed to describe the interaction of the incident light with intimate mixtures, for these mixtures, its performance was not significantly better than that of linear unmixing. An interesting observation is that HPU and SPU performed identically, as did HGU and SGU, indicating that the projection onto the hypersphere or onto the simplex leads to similar results.

D. Experiment on Multisensor Hyperspectral Benchmark Dataset

In the VNIR–SWIR wavelength regions, we utilized the ASD spectroradiometer datasets to train the supervised approaches, and the proposed methods were validated on the dataset acquired by the remaining seven sensors [PSR-3500 spectral evolution, Specim AisaFenix, IMEC hyperspectral camera, Specim sC-MOS, Senops HSC2, Cubert Ultrix X20P, and Specim JAI (RGB)]. In the MWIR–LWIR wavelength regions, the dataset obtained by the spectroradiometer (Agilent 4300 FTIR) served

TABLE IV
AE OF ALL METHODS ON THE BINARY INTIMATE MIXTURES OF THE SELF-CRAFTED MINERAL DATASET

	FCLSU	PPNM	MLM	Hapke	NBRU	HPU	HGU	SPU	**SGU**
Al−Si	48.93	33.20	48.93	48.93	**21.21**	37.28	28.65	37.28	28.65
Ca−Si	59.75	38.90	20.42	59.75	41.90	**3.43**	3.59	**3.43**	3.58
Ca−Ti	15.62	12.60	12.32	15.99	13.68	6.10	**5.77**	6.11	**5.77**
Fe−Al	45.94	47.28	42.82	31.45	40.77	10.65	**8.62**	10.65	**8.62**
Fe−Ca	21.10	32.14	21.01	11.02	10.46	2.63	**1.15**	2.63	**1.15**
Fe−Si	61.02	65.56	59.96	55.57	59.21	**17.70**	25.92	**17.70**	25.92
Si−Ti	61.87	31.32	24.53	61.91	27.85	11.88	**11.41**	11.89	**11.42**

The best performances are shown in bold.

TABLE V
MEAN AE OF ALL METHODS ON THE BINARY INTIMATE MIXTURES OF THE MULTISENSOR HYPERSPECTRAL BENCHMARK DATASET

	FCLSU	PPNM	MLM	Hapke	NBRU	HPU	HGU	SPU	**SGU**
LWIR									
Specim AisaOwl	16.40±7.44	8.91±8.17	15.28±8.66	16.84±7.69	11.01±6.94	10.83±13.30	7.11±3.92	10.39±13.46	**6.64±3.80**
MWIR									
Specim FX50	16.44±8.23	14.45±6.66	12.51±6.15	22.61±11.12	11.18±4.18	7.21±5.01	7.35±4.78	**6.89±4.98**	7.05±4.79
VNIR									
Specim sCMOS	6.56±4.23	6.17±2.61	9.16±3.17	22.04±10.45	17.32±9.19	6.17±5.79	**5.64±4.81**	6.19±5.78	5.65±4.85
Cubert Ultris X20P	34.07±15.25	34.87±11.13	35.88±16.29	36.28±14.63	40.86±10.65	37.98±16.43	23.03±7.91	38.02±16.42	**23.00±7.95**
Specim JAI(RGB)	8.25±6.95	9.69±3.98	7.78±4.61	26.17±8.55	11.87±5.71	8.32±4.85	**7.32±2.96**	8.31±4.81	7.34±2.90
Senops HSC2	17.72±9.39	16.74±9.39	18.02±9.35	30.45±9.53	**14.63±8.34**	20.19±9.68	22.27±9.89	20.15±9.66	22.28±9.87
SWIR									
IMEC hyperspectral camera	14.10±15.82	15.28±7.11	9.34±5.58	20.26±14.11	9.76±5.51	**8.77±7.14**	9.11±7.15	8.78±7.14	9.12±7.15
VNIRSWIR									
PSR-3500 spectral evolution	8.14±5.39	**6.28±3.05**	7.58±4.93	17.90±9.16	14.41±7.0	7.76±4.79	7.70±4.77	7.80±4.75	7.73±4.74
Specim AisaFenix	8.74±6.68	6.62±2.45	8.33±4.81	23.09±9.19	23.14±11.09	**5.92±1.63**	6.83±2.28	5.94±1.69	6.81±2.35

The best performances are shown in bold.

as training data, and the unmixing methods were validated using the data from the two imaging sensors (Specim FX50 and Specim AisaOwl). The results of all spectral unmixing techniques applied to this dataset are shown in Table V. Unlike the previous experiments, where the proposed methods or the Hapke model excelled in estimating intimate mixtures, for this dataset, also the linear, bilinear, and MLMs performed effectively, and their performances were comparable to each other. Overall, the best results were consistently obtained by one of the four proposed methods. Specifically, the proposed methods demonstrated superior performance in comparison to the models when estimating the fractional abundances of the intimate mixtures across the seven sensors: Specim AisaOwl, Specim FX50, Specim sCMOS, Cubert Ultrix X20P, Specim JAI(RGB), IMEC hyperspectral camera, and Specim AisaFenix. This demonstrates the robustness and effectiveness of the proposed methods across a diverse range of datasets. PPNM demonstrated superior performance in predicting abundances from the PSR-3500 spectral evolution dataset. On the other hand, NBRU emerged as the top performer on the Senops HSC2 dataset.

V. DISCUSSION

The results of the experiments lead to the following overall conclusions.

1) Generally, the LMM proves unsuitable for accurately describing the spectral reflectances of binary intimate mixtures of mineral powders. Its AE varied between 7% and 62%. Unexpectedly, the model showed good performance on four out of the nine sensors from the multisensor hyperspectral benchmark dataset (see Table V).

2) Similar to the LMM, the bilinear model PPNM did not perform well in estimating the fractional abundances of binary intimate mixtures. In general, its performance was better than the LMM for most of the datasets. Its AE varied between 6.5% and 66%. This implies that this model is not well-suited for characterizing the interaction of light with intimate mixtures.

3) Similar to the PPNM, the MLM outperformed the LMM for predicting the fractional abundances of binary intimate mixtures. However, the obtained AE's remain excessively high, making it unreliable.

4) As mentioned in Section I, for the Hapke model to perform well, the particles of the intimate mixtures have to be larger than the wavelength of the incident light, be spherically shaped, and scatter light isotropically. Among the three datasets studied in this work, only the Relab dataset fulfilled the criteria, resulting in excellent performance. On the remaining two datasets, it could not

outperform the LMM, suggesting less suitability of this model for real-life applications.

5) Even though NBRU performed better than the FCLSU, PPNM, and MLM models on the Relab dataset, its performance on the other datasets was not significantly better than the models.

6) The proposed methods demonstrated strong performance across all binary intimate mixtures. On the majority of mixtures, the projection methods HPU and SPU performed equally well, as did the geodesic approaches HGU and SGU (see Tables III–V). This already eliminates the need of having to choose between the simplex or the hypersphere projection. In this way, the number of models to select from is narrowed down to two, i.e., a projection unmixing (HPU or SPU) and a geodesic unmixing method (HGU or SGU). We should note that we applied these two approaches to several datasets and the differences in the performance were not significant. For most of the intimate mixtures, the differences were between 1% and 2%. Therefore, the best method depends very much on the intimate mixtures. A possible solution is to average results from a projection and a geodesic method (e.g., HPU and HGU).

7) Even though Equations (4) and (5) share a similar structure, their inputs are completely different. Equation (4) relies on true arc lengths, whereas (5) uses approximated geodesic distances to determine the relative position of the binary mixture.

8) The relatively low performance of the proposed methods on the binary mixtures of Al–Si arises from the featureless nature of both minerals, as they exhibit almost identical reflection values across all bands. To reduce random scaling effects in the measured spectral reflectances, the proposed methods involve projecting the data onto the unit hypersphere or the high-dimensional simplex. While this approach effectively addresses spectral variability, it comes at the cost of removing information regarding absolute magnitude. This information is crucial for accurately performing spectral unmixing of mixtures with flat endmember spectra, as the Al–Si mixtures.

9) The poor performance of the proposed methods on Fe–Si mixtures (see Section III-B and Table IV) is due to the unnatural behavior of the measured spectral reflectance of the mixtures. As the spectral reflectances of several mixtures lie outside of the curve connecting the endmembers, these binary mixtures are projected on one of the endmembers, i.e., Fe_2O_3. Fig. 7 shows that the spectra of these mixtures, even the ones with low fractions of Fe_2O_3 resemble the spectrum of pure Fe_2O_3.

10) The reduced performance of the proposed methods on the mixtures acquired by the Cubert Ultris X20P and Senops HSC2 sensors can be attributed to the low quality of the measured spectral reflectances (see [53, discussion section]).

11) Unlike mixing models, the major disadvantage of the proposed methods is that they are supervised. To invert the function F, they require training samples. When a
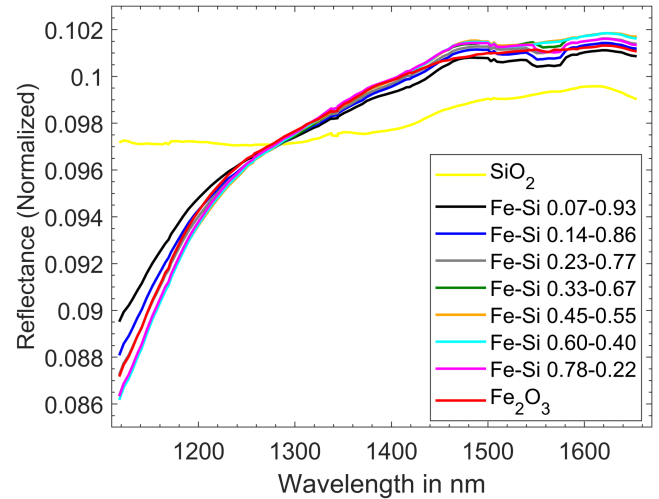

Fig. 7. Spectral reflectance of binary mixtures of Fe_2O_3 and SiO_2 acquired by the hyperspectral camera.

radiative transfer model cannot well explain the interaction of the light with the intimate mixtures, it cannot be used to generate training data, and the training samples should be real data, acquired by a specific sensor. This makes the proposed approaches less suitable for use in remote sensing applications, but this criterion can be easily met in close-range applications in laboratory or industrial settings.

12) The major disadvantage of the proposed method is that it is only suitable for estimating the fractional abundances of binary mixtures. However, in close-range applications, encounters with intimate mixtures of two pure substances are common, a phenomenon extensively explored (refer to [54], for example).

VI. CONCLUSION

This study introduced four distinct supervised methodologies aimed at estimating fractional abundances in binary intimate mixtures. These techniques were specifically developed to tackle nonlinearity and spectral variability simultaneously. The approaches were validated on a large variety of binary mixtures acquired by a wide range of sensors, spanning wavelengths from the visible to the long-wavelength infrared regions. The experimental results confirmed the effectiveness of the proposed methodologies and their superiority over mixing models. In future work, we will explore the feasibility of extending the proposed method to accommodate higher order mixtures.

REFERENCES

[1] N. Keshava and J. F. Mustard, "Spectral unmixing," *IEEE Signal Process. Mag.*, vol. 19, no. 1, pp. 44–57, Jan. 2002.

[2] J. W. Boardman, "Geometric mixture analysis of imaging spectrometry data," in *Proc. IEEE Int. Geosci. Remote Sens. Symp.*, 1994, pp. 2369–2371.

[3] D. C. Heinz and Chein-I-Chang, "Fully constrained least squares linear spectral mixture analysis method for material quantification in hyperspectral imagery," *IEEE Trans. Geosci. Remote Sens.*, vol. 39, no. 3, pp. 529–545, Mar. 2001.

[4] Y. Qu and H. Qi, "uDAS: An untied denoising autoencoder with sparsity for spectral unmixing," *IEEE Trans. Geosci. Remote Sens.*, vol. 57, no. 3, pp. 1698–1712, Mar. 2019.

[5] Y. Su, A. Marinoni, J. Li, J. Plaza, and P. Gamba, "Stacked nonnegative sparse autoencoders for robust hyperspectral unmixing," *IEEE Geosci. Remote Sens. Lett.*, vol. 15, no. 9, pp. 1427–1431, Sep. 2018.

[6] Y. Su, J. Li, A. Plaza, A. Marinoni, P. Gamba, and S. Chakravortty, "DAEN: Deep autoencoder networks for hyperspectral unmixing," *IEEE Trans. Geosci. Remote Sens.*, vol. 57, no. 7, pp. 4309–4321, Jul. 2019.

[7] R. A. Borsoi, T. Imbiriba, and J. C. M. Bermudez, "Deep generative endmember modeling: An application to unsupervised spectral unmixing," *IEEE Trans. Comput. Imag.*, vol. 6, pp. 374–384, 2020.

[8] B. Palsson, M. O. Ulfarsson, and J. R. Sveinsson, "Convolutional autoencoder for spectral-spatial hyperspectral unmixing," *IEEE Trans. Geosci. Remote Sens.*, vol. 59, no. 1, pp. 535–549, Jan. 2021.

[9] L. Gao, Z. Han, D. Hong, B. Zhang, and J. Chanussot, "CyCU-Net: Cycle-consistency unmixing network by learning cascaded autoencoders," *IEEE Trans. Geosci. Remote Sens.*, vol. 60, 2022, Art. no. 5503914.

[10] B. Rasti, B. Koirala, P. Scheunders, and P. Ghamisi, "UnDIP: Hyperspectral unmixing using deep image prior," *IEEE Trans. Geosci. Remote Sens.*, vol. 60, 2022, Art. no. 5504615.

[11] B. Rasti, B. Koirala, P. Scheunders, and J. Chanussot, "MiSiCNet: Minimum simplex convolutional network for deep hyperspectral unmixing," *IEEE Trans. Geosci. Remote Sens.*, vol. 60, 2022, Art. no. 5522815.

[12] Q. Jin, Y. Ma, F. Fan, J. Huang, X. Mei, and J. Ma, "Adversarial autoencoder network for hyperspectral unmixing," *IEEE Trans. Neural Netw. Learn. Syst.*, vol. 34, no. 8, pp. 4555–4569, Aug. 2023.

[13] M. Tang, Y. Qu, and H. Qi, "Hyperspectral nonlinear unmixing via generative adversarial network," in *Proc. IEEE Int. Geosci. Remote Sens. Symp.*, 2020, pp. 2404–2407.

[14] P. Ghosh, S. K. Roy, B. Koirala, B. Rasti, and P. Scheunders, "Hyperspectral unmixing using transformer network," *IEEE Trans. Geosci. Remote Sens.*, vol. 60, 2022, Art. no. 5535116.

[15] Z. Yang, M. Xu, S. Liu, H. Sheng, and J. Wan, "UST-Net: A U-shaped transformer network using shifted windows for hyperspectral unmixing," *IEEE Trans. Geosci. Remote Sens.*, vol. 61, 2023, Art. no. 5528815.

[16] R. Heylen, M. Parente, and P. Gader, "A review of nonlinear hyperspectral unmixing methods," *IEEE J. Sel. Topics Appl. Earth Observ. Remote Sens.*, vol. 7, no. 6, pp. 1844–1868, Jun. 2014.

[17] W. Fan, B. Hu, J. Miller, and M. Li, "Comparative study between a new nonlinear model and common linear model for analysing laboratory simulated-forest hyperspectral data," *Int. J. Remote Sens.*, vol. 30, no. 11, pp. 2951–2962, 2009.

[18] A. Halimi, Y. Altmann, N. Dobigeon, and J. Tourneret, "Nonlinear unmixing of hyperspectral images using a generalized bilinear model," *IEEE Trans. Geosci. Remote Sens.*, vol. 49, no. 11, pp. 4153–4162, Nov. 2011.

[19] Y. Altmann, A. Halimi, N. Dobigeon, and J. Tourneret, "Supervised nonlinear spectral unmixing using a postnonlinear mixing model for hyperspectral imagery," *IEEE Trans. Image Process.*, vol. 21, no. 6, pp. 3017–3025, Jun. 2012.

[20] I. Meganem, P. Déliot, X. Briottet, Y. Deville, and S. Hosseini, "Linear–quadratic mixing model for reflectances in urban environments," *IEEE Trans. Geosci. Remote Sens.*, vol. 52, no. 1, pp. 544–558, Jan. 2014.

[21] R. Heylen and P. Scheunders, "A multilinear mixing model for nonlinear spectral unmixing," *IEEE Trans. Geosci. Remote Sens.*, vol. 54, no. 1, pp. 240–251, Jan. 2016.

[22] A. Marinoni and P. Gamba, "A novel approach for efficient p-linear hyperspectral unmixing," *IEEE J. Sel. Topics Signal Process.*, vol. 9, no. 6, pp. 1156–1168, Sep. 2015.

[23] A. Marinoni, J. Plaza, A. Plaza, and P. Gamba, "Nonlinear hyperspectral unmixing using nonlinearity order estimation and polytope decomposition," *IEEE J. Sel. Topics Appl. Earth Observ. Remote Sens.*, vol. 8, no. 6, pp. 2644–2654, Jun. 2015.

[24] A. Marinoni, A. Plaza, and P. Gamba, "Harmonic mixture modeling for efficient nonlinear hyperspectral unmixing," *IEEE J. Sel. Topics Appl. Earth Observ. Remote Sens.*, vol. 9, no. 9, pp. 4247–4256, Sep. 2016.

[25] B. Hapke, R. Nelson, and W. Smythe, "The opposition effect of the moon: Coherent backscatter and shadow hiding," *Icarus*, vol. 133, no. 1, pp. 89–97, 1998.

[26] B. Hapke, "Bidirectional reflectance spectroscopy: 1. Theory," *J. Geophysical Res.*, vol. 86, pp. 3039–3054, 1981.

[27] M. Zhao, L. Yan, and J. Chen, "LSTM-DNN based autoencoder network for nonlinear hyperspectral image unmixing," *IEEE J. Sel. Topics Signal Process.*, vol. 15, no. 2, pp. 295–309, Feb. 2021.

[28] M. Zhao, M. Wang, J. Chen, and S. Rahardja, "Hyperspectral unmixing for additive nonlinear models with a 3-D-CNN autoencoder network," *IEEE Trans. Geosci. Remote Sens.*, vol. 60, 2022, Art. no. 5509415.

[29] B. Rasti, B. Koirala, and P. Scheunders, "HapkeCNN: Blind nonlinear unmixing for intimate mixtures using Hapke model and convolutional neural network," *IEEE Trans. Geosci. Remote Sens.*, vol. 60, 2022, Art. no. 5536315.

[30] G. Foody, "Relating the land-cover composition of mixed pixels to artificial neural network classification output," *Photogrammetric Eng. Remote Sens.*, vol. 62, no. 5, pp. 491–499, 1996.

[31] G. Licciardi and F. D. Frate, "Pixel unmixing in hyperspectral data by means of neural networks," *IEEE Trans. Geosci. Remote Sens.*, vol. 49, no. 11, pp. 4163–4172, Nov. 2011.

[32] B. Koirala, R. Heylen, and P. Scheunders, "A neural network method for nonlinear hyperspectral unmixing," in *Proc. IEEE Int. Geosci Remote Sens. Symp.*, 2018, pp. 4233–4236.

[33] M. Koirala, B. Khodadadzadeh, C. Contreras, Z. Zahiri, R. Gloaguen, and P. Scheunders, "A supervised method for nonlinear hyperspectral unmixing," *Remote Sens.*, vol. 11, no. 20, Oct. 2019, Art. no. 2458.

[34] B. Koirala, Z. Zahiri, A. Lamberti, and P. Scheunders, "Robust supervised method for nonlinear spectral unmixing accounting for endmember variability," *IEEE Trans. Geosci. Remote Sens.*, vol. 59, no. 9, pp. 7434–7448, Sep. 2021.

[35] L. Drumetz, J. Chanussot, C. Jutten, W. Ma, and A. Iwasaki, "Spectral variability aware blind hyperspectral image unmixing based on convex geometry," *IEEE Trans. Image Process.*, vol. 29, pp. 4568–4582, 2020.

[36] B. Somers, M. Zortea, A. Plaza, and G. P. Asner, "Automated extraction of image-based endmember bundles for improved spectral unmixing," *IEEE J. Sel. Topics Appl. Earth Observ. Remote Sens.*, vol. 5, no. 2, pp. 396–408, Apr. 2012.

[37] T. Uezato, R. J. Murphy, A. Melkumyan, and A. Chlingaryan, "A novel endmember bundle extraction and clustering approach for capturing spectral variability within endmember classes," *IEEE Trans. Geosci. Remote Sens.*, vol. 54, no. 11, pp. 6712–6731, Nov. 2016.

[38] C. A. Bateson, G. P. Asner, and C. A. Wessman, "Endmember bundles: A new approach to incorporating endmember variability into spectral mixture analysis," *IEEE Trans. Geosci. Remote Sens.*, vol. 38, no. 2, pp. 1083–1094, Mar. 2000.

[39] L. Drumetz, M. Veganzones, S. Henrot, R. Phlypo, J. Chanussot, and C. Jutten, "Blind hyperspectral unmixing using an extended linear mixing model to address spectral variability," *IEEE Trans. Image Process.*, vol. 25, no. 8, pp. 3890–3905, Aug. 2016.

[40] P. Thouvenin, N. Dobigeon, and J. Tourneret, "Hyperspectral unmixing with spectral variability using a perturbed linear mixing model," *IEEE Trans. Signal Process.*, vol. 64, no. 2, pp. 525–538, Jan. 2016.

[41] D. Hong, N. Yokoya, J. Chanussot, and X. X. Zhu, "An augmented linear mixing model to address spectral variability for hyperspectral unmixing," *IEEE Trans. Image Process.*, vol. 28, no. 4, pp. 1923–1938, Apr. 2019.

[42] A. Halimi, N. Dobigeon, and J. Tourneret, "Unsupervised unmixing of hyperspectral images accounting for endmember variability," *IEEE Trans. Image Process.*, vol. 24, no. 12, pp. 4904–4917, Dec. 2015.

[43] Y. Zhou, A. Rangarajan, and P. D. Gader, "A Gaussian mixture model representation of endmember variability in hyperspectral unmixing," *IEEE Trans. Image Process.*, vol. 27, no. 5, pp. 2242–2256, May 2018.

[44] Y. Zhou, E. B. Wetherley, and P. D. Gader, "Unmixing urban hyperspectral imagery using probability distributions to represent endmember variability," *Remote Sens. Environ.*, vol. 246, 2020, Art. no. 111857.

[45] T. Uezato, M. Fauvel, and N. Dobigeon, "Hyperspectral unmixing with spectral variability using adaptive bundles and double sparsity," *IEEE Trans. Geosci. Remote Sens.*, vol. 57, no. 6, pp. 3980–3992, Jun. 2019.

[46] A. Halimi, P. Honeine, and J. M. Bioucas-Dias, "Hyperspectral unmixing in presence of endmember variability, nonlinearity, or mismodeling effects," *IEEE Trans. Image Process.*, vol. 25, no. 10, pp. 4565–4579, Oct. 2016.

[47] A. Halimi, J. M. Bioucas-Dias, N. Dobigeon, G. S. Buller, and S. McLaughlin, "Fast hyperspectral unmixing in presence of nonlinearity or mismodeling effects," *IEEE Trans. Comput. Imag.*, vol. 3, no. 2, pp. 146–159, Jun. 2017.

[48] W. Luo, L. Gao, R. Zhang, A. Marinoni, and B. Zhang, "Bilinear normal mixing model for spectral unmixing," *IET Image Process.*, vol. 13, no. 2, pp. 344–354, 2019.

[49] K. Siebels, K. Goïta, and M. Germain, "Estimation of mineral abundance from hyperspectral data using a new supervised neighbor-band ratio unmixing approach," *IEEE Trans. Geosci. Remote Sens.*, vol. 58, no. 10, pp. 6754–6766, Oct. 2020.

[50] B. Koirala, Z. Zahiri, and P. Scheunders, "A robust supervised method for estimating soil moisture content from spectral reflectance," *IEEE Trans. Geosci. Remote Sens.*, vol. 60, 2022, Art. no. 5539813.

[51] C. Rasmussen and C. Williams, *Gaussian Processes for Machine Learning*. New York, NY, USA: MIT Press, 2006.

[52] J. F. Mustard and C. M. Pieters, "Photometric phase functions of common geologic minerals and applications to quantitative analysis of mineral mixture reflectance spectra," *J. Geophysical Res.*, vol. 94, pp. 13619–13634, 1989.

[53] B. Koirala et al., "A multisensor hyperspectral benchmark dataset for unmixing of intimate mixtures," *IEEE Sensors J.*, vol. 24, no. 4, pp. 4694–4710, Feb. 2024.

[54] M. J. d. Oliveira, *Binary Mixtures*. Berlin, Germany: Springer, 2017, pp. 171–200.

Bikram Koirala (Member, IEEE) received the M.S. degree in geomatics engineering from the University of Stuttgart, Stuttgart, Germany, in 2016, and the Ph.D. degree in development of advanced hyperspectral unmixing methods from the University of Antwerp, Antwerp, Belgium, in 2021.

In 2017, he joined the Vision Lab, Department of Physics, University of Antwerp, as a Ph.D. Researcher, where he is currently a Postdoctoral Researcher. His research interests include machine learning and hyperspectral image processing.

Behnood Rasti (Senior Member, IEEE) received the B.Sc. and M.Sc. degrees in electronics and electrical engineering from Electrical Engineering Department, University of Guilan, Rasht, Iran, in 2006 and 2009, respectively, and the Ph.D. degree in electrical and computer engineering from the University of Iceland, Reykjavik, Iceland, in 2014.

He was a Valedictorian as an M.Sc. Student in 2009. In 2015 and 2016, he was a Postdoctoral Researcher with Electrical and Computer Engineering Department, University of Iceland. From 2016 to 2019, he was a Lecturer with the Center of Engineering Technology and Applied Sciences, Department of Electrical and Computer Engineering, University of Iceland. From 2022 to 2023, he was a Principal Research Associate with Helmholtz-Zentrum Dresden-Rossendorf (HZDR), Dresden, Germany. He is currently a Senior Research Scientist with Faculty of Electrical Engineering and Computer Science, Technische Universitt Berlin. His research interests include signal and image processing, machine/deep learning, remote sensing, and artificial intelligence.

Dr. Rasti was a Humboldt Research Fellow in 2020 and 2021. He was the recipient of the Doctoral Grant of the University of Iceland Research Fund "The Eimskip University Fund" and the "Alexander von Humboldt Research Fellowship Grant" in 2013 and 2019, respectively. He is an Associate Editor for IEEE GEOSCIENCE AND REMOTE SENSING LETTERS (GRSL).

Paul Scheunders (Senior Member, IEEE) received the M.S. and Ph.D. degrees in physics, with work in the field of statistical mechanics, from the University of Antwerp, Antwerp, Belgium, in 1986 and 1990, respectively.

In 1991, he became a Research Associate with the Vision Lab, Department of Physics, University of Antwerp, where he is currently a Full Professor. He has authored or coauthored more than 200 papers in international journals and proceedings in the field of image processing, pattern recognition, and remote sensing. His current research interest includes remote sensing and hyperspectral image processing.

Dr. Scheunders is currently an Associate Editor for IEEE TRANSACTIONS ON GEOSCIENCE AND REMOTE SENSING and was a program committee member in numerous international conferences. He is a senior member of the IEEE Geoscience and Remote Sensing Society.